MATERIALS SCIENCE

Single-crystalline epitaxial TiO film: A metal and superconductor, similar to Ti metal

Fengmiao Li[1,2]*, Yuting Zou[3,4], Myung-Geun Han[5], Kateryna Foyevtsova[1,2], Hyungki Shin[1,2], Sangjae Lee[6], Chong Liu[1,2], Kidae Shin[7], Stephen D. Albright[6], Ronny Sutarto[8], Feizhou He[8], Bruce A. Davidson[1,2], Frederick J. Walker[7], Charles H. Ahn[6,7], Yimei Zhu[5], Zhi Gang Cheng[3,4,9], Ilya Elfimov[1,2], George A. Sawatzky[1,2]*, Ke Zou[1,2]*

Titanium monoxide (TiO), an important member of the rock salt 3d transition-metal monoxides, has not been studied in the stoichiometric single-crystal form. It has been challenging to prepare stoichiometric TiO due to the highly reactive Ti^{2+}. We adapt a closely lattice-matched MgO(001) substrate and report the successful growth of single-crystalline TiO(001) film using molecular beam epitaxy. This enables a first-time study of stoichiometric TiO thin films, showing that TiO is metal but in proximity to Mott insulating state. We observe a transition to the superconducting phase below 0.5 K close to that of Ti metal. Density functional theory (DFT) and a DFT-based tight-binding model demonstrate the extreme importance of direct Ti–Ti bonding in TiO, suggesting that similar superconductivity exists in TiO and Ti metal. Our work introduces the new concept that TiO behaves more similar to its metal counterpart, distinguishing it from other 3d transition-metal monoxides.

INTRODUCTION

The 3d transition-metal oxides host a large variety of intriguing properties, such as the high-temperature (T_c) superconductivity in copper oxides (*1*), metal-insulator transition in the series of $RNiO_3$ (R, rare earth elements) accompanied by magnetic ordering (*2*), and the colossal magnetoresistance in Mn oxides (*3*). The exceptionally rich physics is mostly derived from the interplay between the charge, lattice, spin, and orbital degrees of freedom (*4*, *5*). Especially important is the strong on-site Coulomb repulsion among 3d electrons of transition-metal cations, bringing about the so-called strongly correlated electron system in which the single-particle physics fails.

The 3d transition-metal monoxides, including TiO, VO, (CrO), MnO, FeO, CoO, NiO, and (CuO), have the simple rock salt structure (inset of Fig. 1), with the well-known exceptions of CrO and CuO and similar lattice constant. The rest of the series have played an important role in the development of the physics of strongly correlated systems, serving as a platform to systematically investigate the correlation between their physical properties and the on-site d-d electron Coulomb repulsion energy U_{dd}, which increases monotonically from Ti to Cu due to the contraction of the 3d orbital. The commonly used form of this parameter, effective Coulomb repulsion U_{eff}, is defined as the lowest ionization potential minus the highest electron affinity of a state with n d electrons, where n is the number of 3d electrons in transition-metal cation. The influence of the spin and the orbital occupation determined by the crystal and ligand fields results in a rather nonmonotonic variation of U_{eff} as shown in Fig. 1. This includes the Hund's rule exchange interaction J (0.5 to 0.7 eV) and equals to $U_{dd} + 4J$ for a half-filled shell-like Mn^{2+} in MnO but is reduced to $U_{dd} - J$ for all other fillings (*6*, *7*). The competition between the effective Coulomb repulsion U_{eff} and the kinetic energy of the d electrons characterized by the one-electron band width W_d determines whether the material with integer number of partially occupied d states is an insulator ($U_{eff} > W_d$) or a metal ($U_{eff} < W_d$). All of the 3d transition-metal oxides in the rock salt structure (or with small distortions) are insulators at low temperatures with one possible exception and that is TiO as demonstrated by studies of powder samples (*8*–*10*).

According to the Zaanen-Sawatzky-Allen scheme (*11*), the conductivity bandgap can be either of the Mott-Hubbard type (e.g., VO) with valence and conduction bands of 3d character or of the charge-transfer type (e.g., NiO) with valence band of O 2p and conduction bands of 3d character. The relative size of U_{eff} and the charge-transfer energy Δ_{CT} (defined as the energy cost of exciting an oxygen 2p electron to the cation 3d state) determines the nature of the insulating gap. $U_{eff} < \Delta_{CT}$ indicates a d–d gap and a Mott

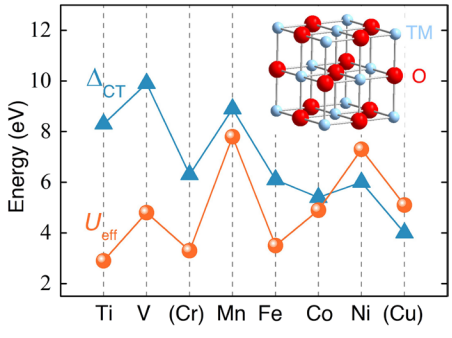

Fig. 1. The series of 3d transition-metal monoxides. The characteristic value of the effective d electron Coulomb repulsion U_{eff} and the charge-transfer energy Δ_{CT} in 3d transition-metal monoxides [adapted from (*7*)]. Inset shows the rock salt structure of 3d transition metal monoxides. TM, 3d transition metal.

[1]Department of Physics and Astronomy, University of British Columbia, Vancouver, British Columbia V6T 1Z1, Canada. [2]Quantum Matter Institute, University of British Columbia, Vancouver, British Columbia V6T 1Z4, Canada. [3]Beijing National Laboratory for Condensed Matter Physics and Institute of Physics, Chinese Academy of Sciences, Beijing 100190, China. [4]School of Physical Sciences, University of Chinese Academy of Sciences, Beijing 100049, China. [5]Condensed Matter Physics and Materials Science Department, Brookhaven National Laboratory, Upton, NY 11973, USA. [6]Department of Physics, Yale University, New Haven, CT 06520, USA. [7]Department of Applied Physics, Yale University, New Haven, CT 06520, USA. [8]Canadian Light Source, Saskatoon, Saskatchewan S7N 2V3, Canada. [9]Songshan Lake Materials Laboratory, Dongguan, Guangdong 523808, China.
*Corresponding author. Email: fengmiao.li@qmi.ubc.ca (F.L.); sawatzky@physics.ubc.ca (G.A.S.); kzou@phas.ubc.ca (K.Z.)

insulator, while $U_{eff} > \Delta_{CT}$ gives the p-d–type gap of a charge-transfer insulator (*11*). The increasing positive nuclear charge Z from Ti to Cu lowers the d state level, and one would expect the monotonic decrease in Δ_{CT}. However, the orbital occupation of the d states and the net spin has also to be considered, causing a nonmonotonic behavior of Δ_{CT} as shown in Fig. 1 (*7*). Upon this consideration, TiO would be a Mott insulator, while NiO would be classified to be a charge-transfer insulator.

The prediction of TiO properties has been difficult. It is well known that the 3d orbitals split into t_{2g} and e_g bands in an octahedral coordination of O as in the rock salt structure. The e_g orbitals with lobes pointing toward the oxygen hybridize strongly with the O 2p orbitals, while the t_{2g} orbitals with orbital lobes pointing between the oxygen have a much weaker hybridization with oxygen. Therefore, the bandwidth resulted from the indirect hopping via oxygen would be rather broad for e_g band and narrow for t_{2g} band. Realizing that the d states closest to the chemical potential are of e_g character in the insulating NiO while they are of t_{2g} character in TiO, we may have expected TiO to be an insulator as well. This would be the case in a perovskite structure, for example, the Mott-insulator $LaTiO_3$, where the nearest-neighbor Ti–Ti distance is very large and the t_{2g} bandwidth is narrow ~2.0 eV (*12*, *13*) and mainly determined by the indirect hoping via oxygen (Ti–O–Ti) rather than the direct Ti–Ti d–d hoping. However, the direct d-d hoping in the rock salt structure is strongly enhanced because of the short distance of nearest-neighbor Ti atoms and results in a larger t_{2g} bandwidth and the almost equal U_{eff} and W_d, making it hard to decide whether TiO would be a Mott insulator or metal.

We need experimental information about the properties and electronic structure of single-crystalline stoichiometric TiO. However, inconsistent results have been reported on the nature of TiO, showing different temperature-dependent resistivities (*8*–*10*, *14*–*16*) and superconductivities with a wide-range of transition temperature T_c from below 0.5 K up to ~7 K (*14*, *15*, *17*–*22*). The main problem in experiment is the strong tendency of Ti^{2+} to form Ti^{3+} or Ti^{4+}, and so achieving high-quality single-crystal TiO is difficult. The recently reported TiO(111) films with superconducting T_c ~ 7 K and their α-Al_2O_3(0001) substrates (*19*–*22*) have the well-known "polar catastrophe" problem (*23*) resulting in the formation of domain structures (*22*) and probable change of stoichiometry from TiO, which leaves the origin of observed superconductivity an open question. The nature of the TiO ground state and whether the reported superconductivity is intrinsic remains a long standing but rather important question in condensed matter physics. In this work, benefited from the well-controlled oxygen pressure and the epitaxy stabilization provided by the lattice-matched nonpolar substrate surface and the epitaxial growth along a nonpolar direction, we have prepared stoichiometric and highly crystalline TiO(001) thin films using oxide molecular beam epitaxy (MBE) on MgO(001) substrates. Unlike the previous bulk powder samples (*8*–*10*, *14*–*18*) and thin films grown along a polar direction (*19*–*22*), our epitaxial thin films are single phase and single domain, allowing transport measurements to reveal the intrinsic properties of TiO.

RESULTS

Thin film growth, structure, and stoichiometry

High-quality TiO(001) films have been prepared using MBE on MgO(001) substrates, which have less than 1% lattice mismatch and provide the lattice-matching template to stabilize the stoichiometric TiO (see Materials and Methods for the growth details). Owing to the strong tendency of forming Ti^{3+} and Ti^{4+} instead of Ti^{2+}, the oxygen pressure in the growth chamber is maintained at ~5.0×10^{-9} torr during film growth and is precisely controlled within a small pressure window of ±1.0×10^{-10} torr, to enable the persistent observation of a single rock salt phase and intensity oscillation in reflection high-energy electron diffraction (RHEED) spots, indicating layer-by-layer growth of atomically smooth, single-domain films. The precise control of oxygen pressure, the extremely low chamber base pressure (less than 1.0×10^{-11} torr, much lower than any other growth method used for TiO), and the epitaxial stabilization provided by the nonpolar MgO substrate surface and the epitaxial growth along the nonpolar <001> direction are the main advantages of the MBE growth method, compared to the bulk samples (*8*–*10*, *14*–*18*) and the films grown by pulsed laser deposition (PLD) (*19*–*22*). As shown in Fig. 2A, RHEED intensity exhibits oscillations at the beginning of growth, which persists during the entire TiO film growth process (fig. S1). The sharp specular and diffracted spots seen on the RHEED patterns of 30-nm sample surface in Fig. 2 (B and C) demonstrate the high crystallinity of the film.

The crystal structures of the TiO films are further characterized by in situ x-ray diffraction (XRD) and ex situ scanning transmission electron microscope (STEM) (see Materials and Methods). The in situ synchrotron surface XRD (SXRD) in Fig. 2D shows a strong TiO(002) diffraction peak on the right side of MgO(002) diffraction with clear finite-thickness fringes, which suggests a sharp interface between MgO and TiO and an atomically smooth TiO surface. Fitting the SXRD data gives the out-of-plane lattice constant of ~4.10 Å, slightly (~2%) smaller than the bulk one (4.18 Å) due to the in-plane tensile strain subjected by the MgO substrate. The coherent growth of TiO on MgO is confirmed by the reciprocal space mapping around the (113) diffraction (fig. S2). The uniformity in TiO film without domains or different phases is manifested by the homogenous contrast seen in the high-angle annular dark-field (HAADF) image in Fig. 2E. The Ti and Mg atom columns in the rock salt lattice are clearly resolved in STEM image (Fig. 2F). In addition, the Ti 2p x-ray photoemission spectroscopy (XPS; fig. S3), Ti $L_{2,3}$ x-ray absorption spectroscopy (XAS; fig. S4), and electron energy loss spectroscopy (EELS; fig. S5) of Ti $L_{2,3}$ show the Ti 2+ valence, which is markedly different from the 3+ and 4+ Ti core level spectra but resembles that of Ti in Ti metal, which also has about two 3d electrons per Ti atom. The pure Ti 2+ valence from the surface-sensitive XPS and bulk-sensitive XAS in total fluorescence mode, together with the persistent RHEED intensity oscillations and the STEM and XRD results, demonstrate the high quality of the film, and the Ti and O ratio in the film is close to 1. In contrast to the case of powder sample (*14*), TiO(001) film epitaxial growth starts with a vacancy-free MgO surface so that the well-defined registry of the substrate and epitaxial thin film, i.e., deposited cation (anion) always sitting on anion (cation) of the substrate, could effectively minimize the defect formation.

Transport properties and superconductivity of TiO

Figure 3A shows the TiO films' resistivity as a function of temperature. The resistivity is ~300 microhm·cm at room temperature, two orders of magnitude higher than Ti metal, and has a weak temperature dependence with a negative derivative on cooling down to 2 K. In principle, TiO can be viewed as a semiconductor with a very

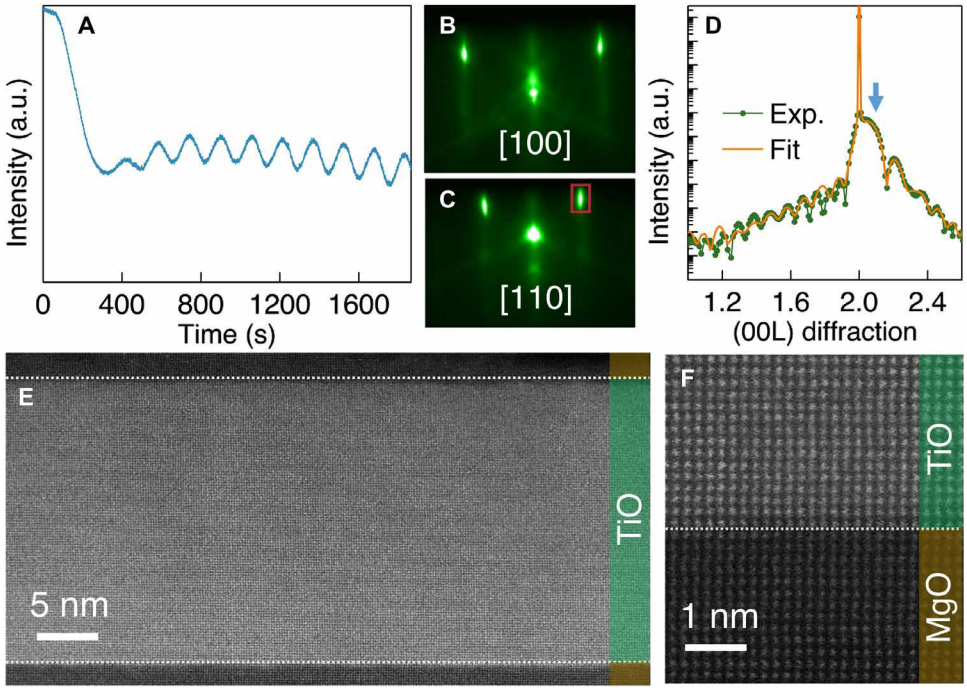

Fig. 2. TiO film growth and its structure and stoichiometry. (**A**) RHEED intensity oscillations of the diffraction spot as marked by rectangle in (C) at the beginning of growth. The intensity oscillation persists during the entire film growth process (fig. S1). (**B** and **C**) RHEED patterns of 30-nm film surface with the incident beam along [100] and [110] direction of MgO substrate, respectively. (**D**) In situ surface x-ray diffraction (SXRD) result of films with a thickness of 10 unit cells and the theoretical fitting. The arrow points to the (002) diffraction peak of TiO film. The large-range (**E**) and small-range (**F**) of the high-angle annular dark-field (HAADF) images of STEM collected on TiO/MgO sample. The white dotted line marks the interface of TiO film and MgO substrate or MgO capping layer. (F) The Mg and Ti columns in MgO substrate and TiO film are clearly resolved. a.u., arbitrary units.

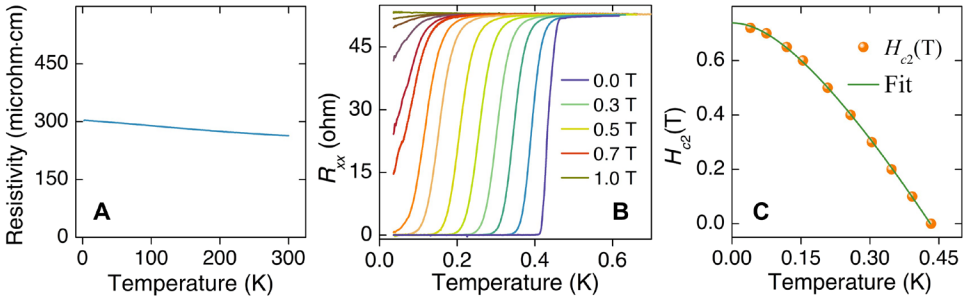

Fig. 3. Transport properties and superconductivity of TiO. (**A**) Resistivity as a function of temperature T from 300 to 2 K in a 50–unit cell–thick TiO film. (**B**) Longitudinal resistance $R_{xx}(T)$ as a function of magnetic field perpendicular to film surface with $T < 0.6$ K. Similar results have been extracted from multiple samples. (**C**) The upper critical field H_{c2} (in tesla) is obtained using 50% criterion of the normal-state resistance value in (B). $H_{c2}(0)$ is extracted from the fitting of H_{c2} (in tesla) with the Werthamer-Helfand-Hohenberg (WHH) model (*25*).

small bandgap due to the negative derivative. Nevertheless, the value of resistivity is much lower than that of most archetypal semiconductors but closer to the metal one, and we do not see the characteristic of bad metal, the resistivity unsaturation (*24*). So, we will describe TiO as a metal. We note that Ti metal has contributions to the conductivity from a broad 4s band crossing the Fermi level strongly hybridized with the Ti 3d bands probably resulting in the much lower resistivity. Unlike the other 3d transition-metal monoxides, TiO does not have any metal-semiconductor transition at a temperature between 2 and 300 K. The higher resistivity than that of most good metals and the slight resistivity increase at low temperature could be indications of being close to a Mott transition with strong fluctuations in local magnetic moments, which will be discussed later in theory part. TiO is not a Mott insulator as suggested by the large Δ_{CT}, an exception in the series of 3d transition-metal monoxides since all the other monoxides show the metal-semiconductor transition or remain insulating to high temperatures.

In the measurements carried out at dilution fridge temperatures, a superconducting transition emerges at $T_c \sim 0.45$ K. Multiple samples show similar superconducting properties. We want to emphasize that TiO is the only superconductor in the series of 3d transition-metal monoxides. As shown in Fig. 3B, the superconducting T_c decreases with increasing applied magnetic field due to the increase in magnetic vortices. The upper critical field H_{c2} (in tesla) in Fig. 3C

is obtained using 50% criterion of the normal-state resistance value. The data fit the Werthamer-Helfand-Hohenberg (WHH) model (*25*) well, yielding $H_{c2}(0) \sim 0.74$ T. We calculate the superconducting Landau-Ginzburg superconducting coherence lengths, $\xi = [(h/2e)/(2\pi H_{c2})]^{1/2} \approx 22$ nm at 0 K. The short electron mean free path suggests TiO is a type II superconductor. We did not observe the higher $T_c \sim 7$ K reported previously in TiO(111) film grown on a sapphire substrate, opening the question as to why the T_c in PLD-grown polar TiO(111) film could be strongly enhanced. The higher T_c is an interesting result and possibly originates from some changes at the observed domains and their boundaries (*22*), e.g., stoichiometry [one example, the γ-Ti_3O_5 phase with $T_c \sim 7$ K (*26*)] or carrier density related to the polar nature of TiO(111) film and the α-Al_2O_3(0001) substrate (*23*). We suggest doing more studies on the TiO(111)/α-Al_2O_3(0001) system, which might lead to some findings unveiling the mystery of the enhanced superconductivity and suggesting a controllable method to increase the T_c of titanium oxide compound.

The T_c of MBE-grown TiO films is close to that of Ti metal $T_c \sim 0.49$ K, although Ti metal is a type I superconductor with a small critical field of 0.01 T. Note that the Ti sublattice in TiO is face-centered cubic (fcc) structure where Ti has 12 Ti nearest neighbors with an interatomic distance very close to that of Ti metal with a hexagonal closed-packed (hcp) structure. We show this comparison in fig. S6 by removing the oxygen atoms from TiO lattice and creating an fcc Ti structure. The similar superconducting T_c and atomic structure between Ti metal and TiO motivated us to investigate their low-energy electronic structure close to the Fermi level and the role of oxygen in TiO theoretically.

Band structure of TiO by density functional theory and tight binding model

The nonspin-polarized density functional theory (DFT) (*27*, *28*) calculations using the generalized gradient approximation (GGA) (*29*) on the rock salt TiO and fcc Ti were performed using the Wien2k code (*30*), and the results are shown in Fig. 4 (A and B). In TiO, the bands crossing the Fermi level have mainly Ti 3d t_{2g} character, while the 3d e_g bands reside at ~2 eV above the Fermi level and the O 2p states lie at ~8 eV below the Fermi level that compares well with Δ_{CT} in Fig. 1. The t_{2g} band has a large maximum bandwidth of ~5 eV. To compare with U_{eff}, one could better use the second moment as a measure of the effective band width due to the large variations in the density of the states (DOS) as seen in Fig. 4A. The calculated effective t_{2g} band width W_d is 2.5 eV, only ~0.5 eV smaller than $U_{eff} \sim 3.0$ eV in Fig. 1. This close proximity to the Mott insulating state explains the slight resistivity increase in TiO at low temperature.

As shown in Fig. 4B, the removal of oxygen in TiO (i.e., fcc Ti metal) lowers the 4s band, which now crosses the Fermi level and decreases the separation of the t_{2g} and e_g bands, i.e., the ligand and crystal field splitting. The hybridization of Ti 3d and 4s bands distort the band structure in the regions where the 4s band is close to the d bands and leads to a broad Ti 3d t_{2g} and e_g bandwidth of ~4.0 eV. In contrast to the case of Cu metal, Ti 4s band above E_F + 4 eV still has 3d t_{2g} orbital character, showing the stronger 4s-3d hybridization in Ti metal. Calculations in fig. S7 show the similar broad Ti 3d bandwidth in fcc Ti and the actual Ti metal with hcp structure, suggesting that electrons in Ti metal are less correlated than in TiO. However, a large resemblance of band dispersion close to the Fermi level between TiO and Ti, especially from *X* to *W* points, is clear.

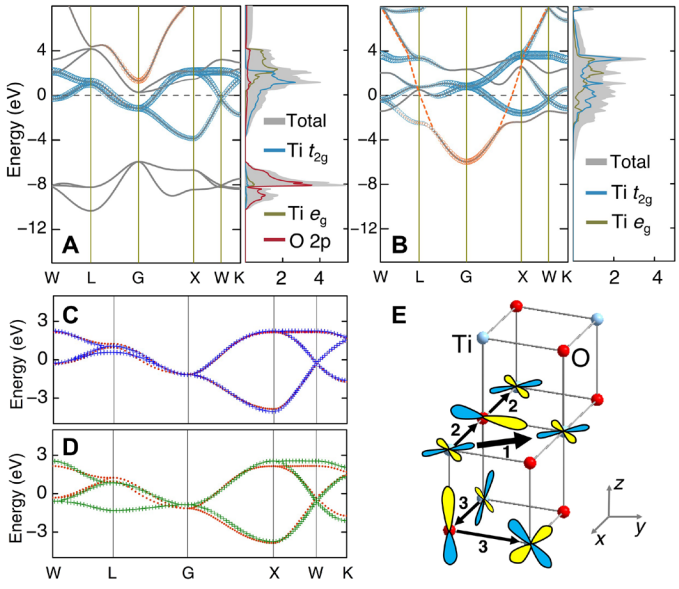

Fig. 4. The low-energy electronic structure of TiO and Ti metal. (**A**) TiO and (**B**) fcc Ti metal band structure and DOS (unit: state per electron volt per TiO) calculated by DFT. The Ti 3d bands with t_{2g} symmetry and Ti 4s band are highlighted by the blue and orange circles, respectively. The orange parabola-like band in (B) represents an artist conception showing the free electron–like dispersion of Ti 4s electron. (**C** and **D**) Tight-binding calculations of TiO include the direct Ti 3d t_{2g} hopping to the nearest-neighbor Ti with (C; blue crosses) and without (D; green crosses) the indirect hopping via oxygen to the nearest-neighbor and next nearest-neighbor Ti, respectively. The red dots represent the DFT-calculated t_{2g} band dispersion. Note that the three O 2p band dispersions are not shown. (**E**) Sketch of the major interactions in TiO. Path #1, Ti $3d_{xy}$ electron directly hopping to the nearest-neighbor Ti $3d_{xy}$; path #2, the 180° bond angle indirect hopping—Ti $3d_{xy}$ via O $2p_y$ orbital to the next nearest-neighbor Ti $3d_{xy}$; path #3, the 90° bond angle indirect hopping—Ti $3d_{xz}$ via O $2p_z$ orbital to the next nearest-neighbor Ti $3d_{yz}$.

To elucidate the major interactions determining the TiO electronic structure at the Fermi level, we have adopted the tight-binding model in which the hopping parameters are derived from the Wannier function fitting of the DFT-calculated band structure (*31*–*33*). We obtain excellent agreement (fig. S8) between the DFT band structure and the band structure from Wannier function fitting using five Ti 3d orbitals and three O 2p orbitals as basis (i.e., including d-d and d-p hopping), in which the direct t_{2g} hopping of nearest-neighbor Ti, e.g., d_{xy}-d_{xy}, is −0.61 eV with *x*, *y*, and *z* unit vector along the cube Ti–O bond directions. In Fig. 4C, the TiO tight-binding calculation reproduces the DFT 3d t_{2g} band dispersion quite accurately, using only the Slater-Koster hopping parameters (*33*) of nearest-neighbor atoms $t_{dd\sigma} = -0.81$ eV, $t_{dd\pi} = 0.36$ eV, $t_{dd\delta} = 0$ eV, $t_{pd\pi} = 0.98$ eV derived from Wannier function fittings, where the $t_{dd\sigma}$ is defined as the integral of d_z^2 hopping to d_z^2 atom orbitals and the definition of other matrix elements between atomic orbitals can be found in (*34*). The tight-binding calculation in Fig. 4D only includes the direct hopping of the nearest-neighbor Ti t_{2g} electron and reproduces most of the band dispersion in DFT except one of the three t_{2g} bands at the L point. The common edge-shared rock salt structure and the short Ti–Ti distance along the diagonal direction (i.e., the nearest-neighbor Ti), as the "direct" hopping schematically

shown by path #1 of Fig. 4E, make the direct Ti 3d t_{2g} electron hopping the dominant mechanism for TiO's low-energy electronic structure, leading to the large resemblance of t_{2g} band dispersions in TiO and Ti metal.

Besides the above Ti 3d direct hopping, Ti 3d electrons could hop to 3d orbitals of another neighboring Ti via the common-shared O 2p orbital, i.e., so-called indirect hopping. The indirect hopping via oxygen Ti-O-Ti to the nearest-neighbor Ti and to the next nearest-neighbor Ti in this common edge-shared structure (i.e., the effective d-d hopping) follows bond angles of 180° (the next nearest-neighbor Ti, e.g., path #2 of Fig. 4E) and 90° (the nearest-neighbor Ti, e.g., path #3 of Fig. 4E), respectively. The effective d-d hopping is given by $t_{dd}^{eff} = -\frac{t_{pd\pi}^2}{\Delta_{CT}} \approx -0.11$ eV in perturbation theory. The comparison of the tight-binding calculation with/without d-p hopping (Fig. 4, C and D) shows that the indirect hopping of t_{2g} electron decreases the eigenvalue of one of the three t_{2g} bands at L point by ~1 eV lowering this band at L point from above to below the Fermi level but has small effect in other regions of reciprocal space and other two t_{2g} bands.

The magnetic ground state in this system is determined by the competition of the direct exchange interaction of Ti d-d direct hopping and the superexchange interactions via oxygen. The calculated superexchange interaction in TiO from equation $J_{dd} \approx \frac{2\left(t_{dd}^{eff}\right)^2}{U_{eff}} = \frac{2t_{pd\pi}^4}{\Delta_{CT}^2 U_{eff}}$ is ~9 meV (*35*) for both 90° and 180° bond angle ones, more than one order of magnitude smaller than in cuprates. The indirect Ti t_{2g} hopping via oxygen depends on the planes of orbitals involved as schematically shown in Fig. 4E. If both Ti's 3d t_{2g} orbitals and the common O 2p orbital are in the same plane, then the superexchange interaction with 180° bond angle is effective (e.g., Ti d_{xy}–Ti d_{xy} hopping via the common O $2p_y$, path #2 of Fig. 4E), while the 90° one is zero. If the two Ti's t_{2g} orbitals reside at a different plane, taking the d_{xz} orbital in one Ti and d_{yz} orbital in another Ti as an example, then the 90° superexchange interaction occurs via the common O $2p_z$ orbital (path #3 of Fig. 4E), but the 180° one is forbidden. In addition, the actual superexchange interaction is only operative if the two t_{2g} orbitals involved on the different Ti atoms are singly occupied. This would result in a potentially complicated orbital ordering pattern in the magnetically ordered phase or complicated short-range spin fluctuation patterns, which could explain the TiO's higher resistivity than that of most good metals. Furthermore, the direct exchange between the nearest-neighbor Ti could be substantial because it involves the large direct d-d hoping integral, which, as demonstrated above, dominates the band structure. However, a perturbative treatment may not work to obtain the superexchange interaction leaving its influence an open question in TiO.

DISCUSSION

Comparing the low-energy electronic structure and superconductivity in TiO and its metal counterpart provides us with a new perspective to study the superconducting mechanisms in transition-metal oxides. Magnon-mediated superconductivity of TiO is unlikely due to the absence of long-range magnetic order in this system, although magnetic susceptibility measurements are still absent and difficult to perform on these thin-film samples. Electron-phonon coupling would play a nontrivial role in the formation of Cooper pairs, which denotes TiO as a conventional superconductor. However, t_{2g} electrons in TiO would interact weakly with O vibration due to the rather weak π bonding relative to, for example, a σ-type bonding in the cuprates, while the Ti atoms' own vibration could be important in the formation of Cooper pairs. TiO and Ti host similar low-energy electronic structures, and both systems have weak t_{2g} electron coupling with oxygen vibrational mode, suggesting a similar pairing mechanism in TiO and Ti metal. However, the Ti 3d-projected partial DOS in fig. S7 shows some difference at the chemical potential in Ti metal and TiO, indicating that the effect of oxygen on the TiO superconductivity is not negligible and needs further investigation.

One interesting question is how the superconductivity in TiO evolves with the free carrier density. The answer to this question will facilitate the understanding of TiO superconductivity and will possibly lead to higher T_c because of the strong variation of the DOS close to E_F. We suggest two feasible experimental methods, electrical gating and chemical substitution, to explore the superconductivity behavior upon the variation of carrier density. (i) One could fabricate high-quality MgO/TiO/MgO sandwich structures, and the top or backside gating on it would make it possible to change the carrier level. (ii) Rock salt TiN also has a very similar t_{2g} band dispersion with TiO (*36*) but a lower Fermi level position due to N preferring to be 3− valence, which is compensated by removing electrons from the Ti 3d band. So, the N substitution of O in TiO will rigidly shift the Fermi level to lower energy and introduce hole carriers.

In conclusion, our work has resolved the long-existing question on the ground state of crystalline stoichiometric TiO, which is a metal but close to the insulating state due to the almost equal U_{eff} and W_d and the expected strong local magnetic momentum fluctuations, and also a superconductor. The successful preparation of high-quality TiO films using MBE enables us to convincingly show these properties. TiO is the only superconductor in this series of 3d transition-metal monoxides oxides with a T_c of ~0.5 K, similar to Ti metal, making it unique. The DFT and tight-binding calculations demonstrate that its uniqueness mainly originates from the importance of Ti–Ti metal bonding that can also explain the large resemblance of core-level spectroscopies such as XPS, XAS, and EELS in TiO and Ti metal, making TiO quite similar to Ti metal in many aspects. These large similarities lead to the similar superconducting T_c. TiO as an epitaxial thin film, a new superconductor, resembles Ti metal but distinguishes itself in various aspects, with many open questions such as: Why is the critical magnetic field difference so large? What is the temperature dependence of the magnetic susceptibility of TiO? Does TiO exhibit strong local magnetic correlations? Is there evidence of local orbital ordering due to nature of the superexchange interactions? Can T_c be increased by electrical gating or anion substitution? And does such doping strongly shift the chemical potential?

MATERIALS AND METHODS

MBE film growth

MgO(001) substrates were annealed at 600°C in ultrahigh vacuum in the MBE chamber before film growth to remove the hydrocarbon contamination. Ti was evaporated by a high-temperature effusion cell with the flux of ~7×10^{12} atoms cm^{-2} s^{-1} calibrated by the quartz crystal microbalance at the growth position. The film was grown with the substrate temperature at 450°C in an O_2 environment with ~5.0×10^{-9} torr pressure from a "three-step procedure" (see the

Supplementary Materials). The O_2 leak valve was adjusted during film growth to maintain constant oxygen partial pressure monitored using a mass spectrometer (Residual Gas Analyzer, SRS-100).

In situ XPS and XAS

The in situ XPS was performed at room temperature in the analysis chamber connected to the MBE growth chamber at the Surface Science Facility of Resonant Elastic and Inelastic X-Ray Scattering (REIXS) beamline of Canadian Light Source. The x-ray source was monochromatized Al Kα radiation ($h\nu$ = 1486.6 eV) with the energy resolution of ~0.4 eV. Because TiO film is insulated from ground by MgO substrate, the electron flood gun needs to be used to compensate charging of the sample resulted from the electron loss during photoemission experiment, and the binding energy was corrected by referencing to the TiO Fermi level. TiO films prepared in the MBE chamber were transferred to the x-ray scattering chamber at the beamline using a vacuum suitcase with vacuum less than 1.0×10^{-9} torr. The REIXS beamline has a flux of 5×10^{12} photons s^{-1} and a photon energy resolution of 10^{-4} eV. The pressure of the chamber during XAS measurement was kept lower than 1.0×10^{-9} torr. The XAS spectra were collected using total fluorescence yield method at room temperature, and the incident angle of the x-ray photon was set to 30° from the sample surface.

Scanning transmission electron microscope

For STEM, the 8 nm MgO-capped 20 nm TiO films on MgO(001) substrate were cross-sectioned by focused ion beam technique using 5 keV Ga^+ ions to minimize ion beam–induced damages. A JEOL ARM 200CF equipped with a cold field emission gun and double spherical aberration correction at Brookhaven National Laboratory operated at 200 kV was used for HAADF imaging with detection angles ranging from 68 to 280 mrad. For EELS, a Gatan Quantum ER spectrometer was used with dispersion (0.1 eV/channel) and ~0.8 eV energy resolution. The convergent and collection semiangles were, respectively, ~10 and ~5 mrad.

In situ SXRD

In situ SXRD measurements of different thicknesses of TiO on MgO substrate were conducted at beam line 33IDE of the Advanced Photon Source, Argonne National Lab using 15-keV photon energy. GenX software (*37*) was used to fit the experimental SXRD curves.

Cryogenic and dilution fridge

Resistivity measurements with temperature from 300 to 2 K were performed in the van der Pauw geometry using a Quantum Design physical property measurement system (PPMS). Indium metal was used as the contact electrode. The film thickness used to obtain the resistivity is from x-ray reflectivity measurement. The superconducting transition was measured by the transport measurements using the Oxford dilution fridge and magnetic fields perpendicular to the sample surface were used. The samples with and without MgO thin-film protection layer show similar resistivity versus temperature and superconducting T_c.

DFT and tight-binding calculations

The Ti metal and TiO electronic structure calculations were performed within DFT using the full-potential linearized-augmented plane-wave code WIEN2k (*30*). The experimental lattice constant of TiO (4.18 Å) was used. We used the GGA method (*29*) to treat exchange and correlation effects. A $20 \times 20 \times 20$ grid of k-points was used for integrating over the Brillouin zone of the $1 \times 1 \times 1$ primitive cell. Projections are made within muffin-tin spheres. The tight-binding calculation was conducted using the Chinook software (*38*), and the Slater-Koster hopping parameters (*33*, *34*) were derived from Wannier function fittings.

SUPPLEMENTARY MATERIALS

Supplementary material for this article is available at http://advances.sciencemag.org/cgi/content/full/7/2/eabd4248/DC1

REFERENCES AND NOTES

1. J. G. Bednorz, K. A. Müller, Possible highT_c superconductivity in the Ba–La–Cu–O system. *Zeitschrift für Phys. B Condens. Matter.* **64**, 189–193 (1986).
2. J. B. Torrance, P. Lacorre, A. I. Nazzal, E. J. Ansaldo, C. Niedermayer, Systematic study of insulator-metal transitions in perovskites $RNiO_3$ (R=Pr,Nd,Sm,Eu) due to closing of charge-transfer gap. *Phys. Rev. B.* **45**, 8209–8212 (1992).
3. S. Jin, T. H. Tiefel, M. McCormack, R. A. Fastnacht, R. Ramesh, L. H. Chen, Thousandfold change in resistivity in magnetoresistive La-Ca-Mn-O films. *Science* **264**, 413–415 (1994).
4. D. Khomskii, *Transition Metal Compounds* (Cambridge Univ. Press, 2014).
5. M. Imada, A. Fujimori, Y. Tokura, Metal-insulator transitions. *Rev. Mod. Phys.* **70**, 1039–1263 (1998).
6. D. van der Marel, G. A. Sawatzky, Electron-electron interaction and localization in *d* and *f* transition metals. *Phys. Rev. B.* **37**, 10674–10684 (1988).
7. J. Zaanen, G. A. Sawatzky, Systematics in band gaps and optical spectra of 3D transition metal compounds. *J. Solid State Chem.* **88**, 8–27 (1990).
8. A. D. Pearson, Studies on the lower oxides of titanium*. *J. Phys. Chem. Solids* **5**, 316–327 (1958).
9. S. P. Denker, Electronic properties of titanium monoxide. *J. Appl. Phys.* **37**, 142–149 (1966).
10. F. Rivadulla, J. Fernández-Rossier, M. Garcia-Hernández, M. A. López-Quintela, J. Rivas, J. B. Goodenough, VO: A strongly correlated metal close to a Mott-Hubbard transition. *Phys. Rev. B.* **76**, 205110 (2007).
11. J. Zaanen, G. A. Sawatzky, J. W. Allen, Band gaps and electronic structure of transition-metal compounds. *Phys. Rev. Lett.* **55**, 418–421 (1985).
12. Y. Okimoto, T. Katsufuji, Y. Okada, T. Arima, Y. Tokura, Optical spectra in $(La,Y)TiO_3$: Variation of Mott-Hubbard gap features with change of electron correlation and band filling. *Phys. Rev. B.* **51**, 9581–9588 (1995).
13. E. Pavarini, A. Yamasaki, J. Nuss, O. K. Andersen, How chemistry controls electron localization in $3d^1$ perovskites: A Wannier-function study. *New J. Phys.* **7**, 188 (2005).
14. M. D. Banus, T. B. Reed, A. J. Strauss, Electrical and magnetic properties of TiO and VO. *Phys. Rev. B.* **5**, 2775–2784 (1972).
15. J. K. Hulm, C. K. Jones, R. A. Hein, J. W. Gibson, Superconductivity in the TiO and NbO systems. *J. Low Temp. Phys.* **7**, 291–307 (1972).
16. A. A. Valeeva, A. A. Rempel, A. I. Gusev, Electrical conductivity and magnetic susceptibility of titanium monoxide. *J. Exp. Theor. Phys. Lett.* **73**, 621–625 (2001).
17. J. K. Hulm, C. K. Jones, R. Mazelsky, R. C. Miller, R. A. Hein, J. W. Gibson, in *Proceedings of the IXth International Conference on Low Temperature Physics* (Plenum Press, 1965), p. 600.
18. D. Wang, C. Huang, J. He, X. Che, H. Zhang, F. Huang, Enhanced superconductivity in rock-salt TiO. *ACS Omega* **2**, 1036–1039 (2017).
19. C. Zhang, F. Hao, G. Gao, X. Liu, C. Ma, Y. Lin, Y. Yin, X. Li, Enhanced superconductivity in TiO epitaxial thin films. *npj Quantum Mater.* **2**, 2 (2017).
20. C. Zhang, Y. Fan, Q. Chen, T. Wang, X. Liu, Q. Li, Y. Yin, X. Li, Quantum Griffiths singularities in TiO superconducting thin films with insulating normal states. *NPG Asia Mater.* **11**, 76 (2019).
21. Y. J. Fan, C. Ma, T. Y. Wang, C. Zhang, Q. L. Chen, X. Liu, Z. Q. Wang, Q. Li, Y. W. Yin, X. G. Li, Quantum superconductor-insulator transition in titanium monoxide thin films with a wide range of oxygen contents. *Phys. Rev. B.* **98**, 064501 (2018).
22. Y. Fan, C. Zhang, X. Liu, Y. Lin, G. Gao, C. Ma, Y. Yin, X. Li, Structure and transport properties of titanium oxide (Ti_2O, $TiO_{1+\delta}$, and Ti_3O_5) thin films. *J. Alloys Compd.* **786**, 607–613 (2019).
23. C. Noguera, Polar oxide surfaces. *J. Phys. Condens. Matter* **12**, R367–R410 (2000).
24. N. E. Hussey, K. Takenaka, H. Takagi, Universality of the Mott–Ioffe–Regel limit in metals. *Philos. Mag.* **84**, 2847–2864 (2004).
25. N. R. Werthamer, E. Helfand, P. C. Hohenberg, Temperature and purity dependence of the superconducting critical field, H_{c2}. III. electron spin and spin-orbit effects. *Phys. Rev.* **147**, 295–302 (1966).
26. K. Yoshimatsu, O. Sakata, A. Ohtomo, Superconductivity in Ti_4O_7 and γ-Ti_3O_5 films. *Sci. Rep.* **7**, 12544 (2017).
27. P. Hohenberg, W. Kohn, Inhomogeneous electron gas. *Phys. Rev.* **136**, B864–B871 (1964).

28. W. Kohn, L. J. Sham, Self-consistent equations including exchange and correlation effects. *Phys. Rev.* **140**, A1133–A1138 (1965).
29. J. P. Perdew, K. Burke, M. Ernzerhof, Generalized gradient approximation made simple. *Phys. Rev. Lett.* **77**, 3865–3868 (1996).
30. P. Blaha, K. Schwarz, F. Tran, R. Laskowski, G. K. H. Madsen, L. D. Marks, WIEN2k: An APW+lo program for calculating the properties of solids. *J. Chem. Phys.* **152**, 074101 (2020).
31. A. A. Mostofi, J. R. Yates, Y.-S. Lee, I. Souza, D. Vanderbilt, N. Marzari, wannier90: A tool for obtaining maximally-localised Wannier functions. *Comput. Phys. Commun.* **178**, 685–699 (2008).
32. J. Kuneš, R. Arita, P. Wissgott, A. Toschi, H. Ikeda, K. Held, Wien2wannier: From linearized augmented plane waves to maximally localized Wannier functions. *Comput. Phys. Commun.* **181**, 1888–1895 (2010).
33. J. C. Slater, G. F. Koster, Simplified LCAO method for the periodic potential problem. *Phys. Rev.* **94**, 1498–1524 (1954).
34. W. A. Harrison, in *Electronic Structure and the Properties of Solids: The Physics of the Chemical Bond* (Dover publications Inc., 2019), p. 445.
35. J. Zaanen, G. A. Sawatzky, The electronic structure and superexchange interactions in transition-metal compounds. *Can. J. Phys.* **65**, 1262–1271 (1987).
36. V. Ern, A. C. Switendick, Electronic band structure of TiC, TiN, and TiO. *Phys. Rev.* **137**, A1927–A1936 (1965).
37. M. Björck, G. Andersson, GenX: An extensible x-ray reflectivity refinement program utilizing differential evolution. *J. Appl. Cryst.* **40**, 1174–1178 (2007).
38. R. P. Day, B. Zwartsenberg, I. S. Elfimov, A. Damascelli, Computational framework *chinook* for angle-resolved photoemission spectroscopy. *npj Quantum Mater.* **4**, 54 (2019).
39. J. F. Moulder, W. F. Stickle, P. E. Sobol, K. D. Bomben, *Handbook of X-ray Photoelectron Spectroscopy* (Eden Prairie, 1995).
40. T. Mazza, P. Piseri, G. Bongiorno, L. Ravagnan, M. Amati, M. Devetta, C. Lenardi, M. Coreno, M. de Simone, P. Milani, Probing the chemical reactivity of free titanium clusters by x-ray absorption spectroscopy. *Appl. Phys. A.* **92**, 463–471 (2008).
41. M. Sinha, M. Gupta, P. Jonnard, M. H. Modi, Soft x-ray characterization of ion beam sputtered magnesium oxide (MgO) thin film. *Surf. Interface Anal.* **50**, 1145–1148 (2018).

Acknowledgments: We thank H. Hong for the assistance with synchrotron SXRD experiment. **Funding:** This research was undertaken thanks in part to funding from the Max Planck–UBC–UTokyo Centre for Quantum Materials and the Canada First Research Excellence Fund, Quantum Materials and Future Technologies Program. The work at UBC was also supported by Natural Sciences and Engineering Research Council of Canada (NSERC) and Canada Foundation for Innovation (CFI). The work at CAS was supported by National Key R&D Program of China grant no. 2018YFA0305604 and National Science Foundation of China (NSFC) grant no. 11874403. The work at BNL was supported by the Materials Science and Engineering Divisions, Office of Basic Sciences of the U.S. Department of Energy under contract no. DESC0012704. STEM sample preparation was carried out at the Center for Functional Nanomaterials, Brookhaven National Laboratory. The work at Yale was supported by the U.S. Department of Energy, Office of Science, Office of Basic Energy Sciences under award number DE-SC0019211. Spectroscopy characterizations and part of the film growth were performed at the Canadian Light Source, a national research facility of University of Saskatchewan, which is supported by the Canada Foundation for Innovation (CFI), the Natural Sciences and Engineering Research Council (NSERC), the National Research Council (NRC), the Canadian Institutes of Health Research (CIHR), the Government of Saskatchewan, and the University of Saskatchewan. Use of the Advanced Photon Source for the SXRD experiment was supported by the U.S. Department of Energy, Office of Science, Office of Basic Energy Sciences under contract no. DE-AC02-06CH11357. **Author contributions:** F.L., R.S., F.H., B.A.D., and K.Z. grew the TiO films. F.L. performed the PPMS resistivity measurement. Y. Zou, K.Z., and Z.G.C. conducted the measurement using dilution fridge. M.-G.H. and Y. Zhu prepared the STEM samples and carried out the measurements. H.S., S.L., C.L., K.S., S.D.A., B.A.D., F.J.W., C.H.A., and K.Z. carried out the SXRD experiment. F.L. and H.S. did the SXRD simulation. F.L., R.S., and F.H. conducted the measurements of XPS and XAS. F.L., K.F., and I.E. performed DFT and Wannier function calculations. F.L. did the tight-binding calculation. F.L., C.L., I.E., G.A.S., and K.Z. analyzed the data. All authors contributed to the writing of the manuscript. **Competing interests:** The authors declare that they have no competing interests. **Data and materials availability:** All data needed to evaluate the conclusions in the paper are present in the paper and/or the Supplementary Materials. Additional data related to this paper may be requested from the authors.

Submitted 19 June 2020
Accepted 10 November 2020
Published 8 January 2021
10.1126/sciadv.abd4248

Citation: F. Li, Y. Zou, M.-G. Han, K. Foyevtsova, H. Shin, S. Lee, C. Liu, K. Shin, S. D. Albright, R. Sutarto, F. He, B. A. Davidson, F. J. Walker, C. H. Ahn, Y. Zhu, Z. G. Cheng, I. Elfimov, G. A. Sawatzky, K. Zou, Single-crystalline epitaxial TiO film: A metal and superconductor, similar to Ti metal. *Sci. Adv.* **7**, eabd4248 (2021).